Gamma width of $^{14}O^*(5.17\ MeV)$ and the stellar $^{13}N(p, \gamma)^{14}O$ reaction rate

M. S. Smith,* P. V. Magnus,† K. I. Hahn,‡ R. M. Curley, and P. D. Parker
A. W. Wright Nuclear Structure Laboratory, Yale University, New Haven, Connecticut 06511

T. F. Wang
Lawrence Livermore National Laboratory, Livermore, California 94551

K. E. Rehm and P. B. Fernandez
Argonne National Laboratory, Argonne, Illinois 60439

S. J. Sanders
Department of Physics and Astronomy, University of Kansas, Lawrence, Kansas 66045

A. García§ and E. G. Adelberger
Physics Department, University of Washington, Seattle, Washington 98195
(Received 2 February 1993)

We have determined the γ-ray branching ratio $\Gamma_\gamma/\Gamma_{tot}$ for the first excited state in ^{14}O ($E_x = 5.17$ MeV) to be $(3.1 \pm 1.7) \times 10^{-4}$, corresponding to a γ width of 12 ± 7 eV. This value was determined by measuring the ratio of the $^{14}N(p, n)^{14}O_0$ to $^{14}N(p, n)^{14}O_1$ cross sections via neutron time of flight, and the ratio of $^{14}N(p, n)^{14}O_0$ to $^{14}N(p, n)^{14}O_1(\gamma)^{14}O_0$ cross sections at the same center-of-mass energy by bombarding a hydrogen target with a ^{14}N beam and kinematically distinguishing the $^{14}O_0$ recoils from the two reaction channels. The present value for Γ_γ is consistent with other measurements at the 2-σ level; a weighted mean of all measurements is used to calculate the stellar $^{13}N(p, \gamma)^{14}O$ reaction rate, and thereby determine the temperatures and densities at which the stellar carbon-nitrogen-oxygen (CNO) cycle is converted to the hot CNO cycle.

PACS number(s): 27.20.+n, 25.40.Lw, 95.30.Cq, 98.80.Ft

I. INTRODUCTION

The gravitational potential energy in massive ($M > 2M_\odot$) main-sequence stars is balanced by the nuclear energy produced by hydrogen burning in the stellar core through the CNO cycle, with the reaction sequence [1]

$$^{12}C(p, \gamma)^{13}N(e^+\nu_e)^{13}C(p, \gamma)^{14}N(p, \gamma)^{15}O(e^+\nu_e)^{15}N(p, \alpha)^{12}C\ . \quad (1)$$

At characterisic main-sequence stellar core temperatures of $2 \times 10^6 \lesssim T(K) \lesssim 80 \times 10^6$ [$2 < T_6 < 80$, where $T_6 \equiv T(K)/10^6$] and densities $\rho \approx 150$ g/cm^3, the slowest reaction in the cycle is $^{14}N(p, \gamma)^{15}O$; this reaction rate limits the energy generation rate of the cycle, and results in typically 94% of all the seed nuclei being ^{14}N during equilibrium CNO hydrogen burning [2]. Furthermore, the resulting $^{15}N/^{14}N$ equilibrium abundance ratio is $\sim 10^{-5}$, a factor of ~ 100 lower than that observed in solar system material. The relative abundance of ^{14}N and ^{15}N has been a serious problem, unexplainable through hydrostatic hydrogen burning in the CNO cycle [3, 4].

Additional processing of the ^{14}N seed nuclei can occur at the slightly raised temperatures characteristic of explosive hydrogen burning scenarios during the later stages of stellar evolution, and may account for the observed $^{15}N/^{14}N$ ratio. At temperatures of $T_9 \approx 0.1 - 0.2$ [$T_9 \equiv T(K)/10^9$], characteristic of hydrogen burning in red giants, nova explosions, and supermassive stars, the $^{13}N(p, \gamma)^{14}O$ reaction rate will exceed the ^{13}N e^+-decay rate, and the reaction sequence changes to

*Present address: Oak Ridge National Laboratory, Physics Division, Bldg. 6000, MS-6371, P.O. Box 2008, Oak Ridge, TN 37831-6371.
†Present address: Physics Department, University of Washington, Seattle, WA 98195.
‡Present address: W. K. Kellogg Radiation Laboratory, California Institute of Technology, Pasadena, CA 91125.
§Present address: Lawrence Berkeley Laboratory, University of California, Berkeley, CA 94720.

$$^{12}C(p,\gamma)^{13}N(p,\gamma)^{14}O(e^+\nu_e)^{14}N(p,\gamma)^{15}O(e^+\nu_e)^{15}N(p,\alpha)^{12}C\ , \quad (2)$$

altering the relative abundances of the seed nuclei as the reaction flow bypasses ^{13}C.

At still higher temperatures, the $^{14}N(p,\gamma)^{15}O$ and $^{13}N(p,\gamma)^{14}O$ reaction rates exceed the ^{14}O and ^{15}O e^+-decay rates (with lifetimes $\tau_{14} = 102$ s and $\tau_{15} = 176$ s, respectively). This constitutes the conversion of the CNO cycle to the hot or "β-limited" CNO cycle, in which the energy generation rate of the cycle is limited by the temperature-independent beta decay rates [1]. The order and precise temperature of the conversion to the hot CNO cycle is determined by the $^{13}N(p,\gamma)^{14}O$ stellar reaction rate. This conversion leads to an increase in the stellar energy production rate by a factor of 3–5 which corresponds to the shorter hydrogen burning time scale. Additionally, the waiting point in the cycle is changed from ^{14}N to the ^{14}O and ^{15}O nuclides, changing the relative equilibrium abundances of the CNO seed nuclides and increasing the $^{15}N/^{14}N$ abundance ratio to between 10^{-2} and 1. This conversion may therefore account for the observed solar system abundance ratio through a mixture of CNO and hot CNO burning products [4].

In order to determine the astrophysical sites at which the CNO cycle is converted to the hot CNO cycle, and thus to better understand the energy generation and resulting $^{15}N/^{14}N$ abundance ratio for these sites, it is necessary to determine the $^{13}N(p,\gamma)^{14}O$ reaction rate as a function of temperature. Since the first excited state of ^{14}O at $E_x = 5.169$ MeV is the only resonance which significantly contributes to the $^{13}N(p,\gamma)^{14}O$ reaction rate at nova temperatures ($0.1 < T_9 < 0.5$), this rate may be determined from properties of this ^{14}O resonance. The ^{14}O level diagram and resonance properties are shown in Fig. 1. Wang [6] and Chupp *et al.* [7] measured $^{14}N(^3He, t)^{14}O$ to determine the excitation energy $E_x = 5.169 \pm 0.0018$ MeV (resonance energy $E_r = 545 \pm 1.8$ keV) and the total width $\Gamma_{tot} = 38.1 \pm 1.8$ keV (and therefore the proton width $\Gamma_p \approx \Gamma_{tot}$). Additionally, the $^{14}O_1$ state has a well-established spin-parity of 1^- (Ref. [8]). The largest uncertainty in the reaction rate is due to the γ width of $^{14}O_1$: an accurate experimental determination of this width is crucial because of the linear dependence of the rate on the resonance strength

$$\omega\gamma = \omega\Gamma_p\Gamma_\gamma/\Gamma_{tot} \approx \omega\Gamma_\gamma \text{ (for } \Gamma_{tot} \approx \Gamma_p), \quad (3)$$

where $\omega = (2J_r+1)/(2J_t+1)(2J_i+1)$ and $J_{r,t,i}$ are the spins of the resonance, target, and incident beam, respectively. We have determined $\Gamma_\gamma/\Gamma_{tot}$ by measuring the $^1H(^{14}N, ^{14}O)n$ and $^{14}N(p, n)^{14}O$ reactions at a center-of-mass energy of 11.67 MeV. We used the $^1H(^{14}N, ^{14}O)n$ reaction to measure the ratio of those $^{14}O_0$ formed by γ decay of $^{14}O_1$ to those $^{14}O_0$ formed directly. We then multiplied this ratio by the number of $^{14}O_0/^{14}O_1$ formed (the production cross section ratio) to obtain a value of $\Gamma_\gamma/\Gamma_{tot}$. The production cross section ratio was determined by measuring neutron time-of-flight angular distributions for the $^{14}N(p, n)^{14}O_{0,1}$ reactions. We then calculated the stellar $^{13}N(p,\gamma)^{14}O$ reaction rate with a weighted mean of the present value for Γ_γ and the indirect measurement of Fernandez *et al.* [9], as well as the recent direct $^{13}N(p,\gamma)^{14}O$ measurement of Decrock *et al.* [10] and the ^{14}O Coulomb-dissociation measurements of Motobayashi *et al.* [11] and Kiener *et al.* [12].

II. THE $^1H(^{14}N, ^{14}O)n\gamma$ REACTION

A. Experimental setup

The 175-MeV ^{14}N beam used in the $^1H(^{14}N, ^{14}O)n\ \gamma$ experiment was produced at the ATLAS Superconducting Heavy Ion Accelerator facility at Argonne National Laboratory [13]. The pulsed beam consisted of 350-ps-wide bursts separated by 82.5 ns, corresponding to a linac frequency of 12.125 MHz. A sweeper was employed to accept only every third beam burst, and typical beam currents were 1 particle nA of $^{14}N^{+7}$.

We used self-supporting 850 $\mu g/cm^2$ $(CH_2)_n$ (polypropylene) targets for the $^1H(^{14}N, ^{14}O)n$ measurement, and 650 $\mu g/cm^2$ carbon targets for determining the background from the $^{12}C(^{14}N, ^{14}O)^{12}B$ reaction. We used an 830 $\mu g/cm^2$ CD_2 target to obtain a fo-

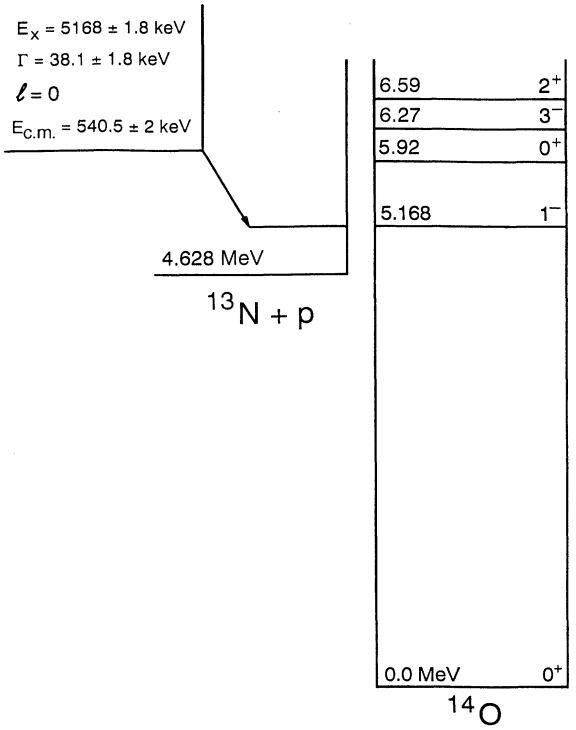

FIG. 1. Level diagram for ^{14}O (Ref. [8]) showing previously measured parameters for the 540-keV $^{13}N + p$ resonance [6, 7]. Energies are in MeV unless otherwise noted.

cal plane position vs momentum calibration with the $^{12}C(^{14}N, ^{14}O)^{12}B$, $^{2}H(^{14}N, ^{15}O)n$, and $^{2}H(^{14}N, ^{14}O)2n$ reactions.

We detected the ^{14}O recoils with an Enge Split Pole magnetic spectrometer positioned at 0° to the beam axis; see Fig. 2. The laboratory opening angles of the spectrometer aperture were $\Theta_x = \pm 2.43°$ (horizontal) and $\Theta_y = \pm 0.74°$ (vertical). We placed a shielded tantalum Faraday cup at the focal plane, to prevent the 10^{10} ^{14}N beam particles/s from entering the detector, and a movable tantalum mask in front of unutilized portions of the detector to further reduce the flux of scattered beam particles. We monitored this beam "halo" to limit the count rate in the focal plane detector to < 100 Hz with an empty target frame and an incident current of 1 particle nA; by comparison, the counting rate for reaction products in the focal plane detector at this beam current was ≈ 1 kHz.

The focal plane detector consisted of a parallel plate avalanche counter (PPAC) backed by a Bragg curve detector (BCD) [14]. The PPAC gives both a fast timing signal (≈ 250 ps) and a position signal (proportional to laboratory momentum P_L) in the horizontal plane, with intrinsic position resolution of 0.75 mm and typical resolution (with windows and target contributions) of 1.0–1.25 mm. We used the Bragg curve detector with standard NIM electronics to measure the total laboratory energy E_L, the range R, and the horizontal entrance angle Θ_x of the incident particles.

B. Data analysis and results

The objective of the $^{1}H(^{14}N, ^{14}O)n$ experiment was to determine the ratio of the number of focal plane events corresponding to $^{14}O_0$'s resulting from the γ decay of $^{14}O_1$ to the ($\sim 10^4$ times larger) number of $^{14}O_0$'s formed directly. This was done in three steps: first by separating out ^{14}O events from those of other particles; second by separating the two ^{14}O groups on the basis of their differing kinematics; and third by summing over the appropriate peaks in their respective momentum spectra.

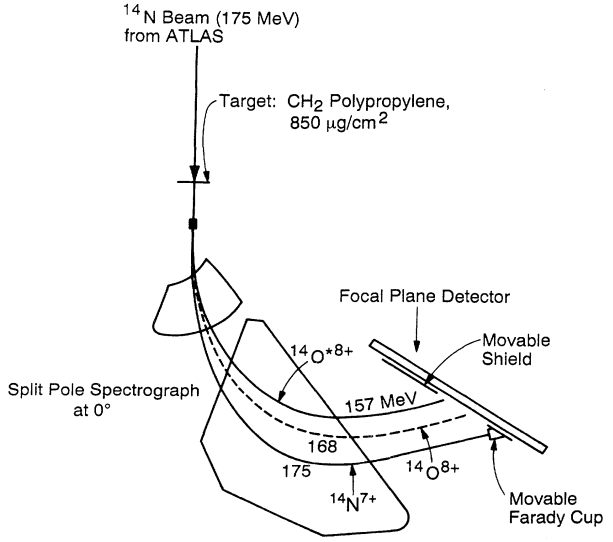

FIG. 2. Experimental setup at ATLAS for the $^{1}H(^{14}N, ^{14}O)n$ measurement. The orbits (and energies in MeV) of the $^{14}N^{+7}$, $^{14}O^{+8}$, and $^{14}O_1(\gamma)^{14}O_0^{+8}$ particles in the 0° Enge split pole magnetic spectrometer are schematically indicated.

In the first step, we separated oxygen events from those of other elements by making a software selection of events in the correct region of the energy-range ($E_L^2 \otimes R$) space, since $R \propto E_L^2/(Z^2A)$, where Z and A are the nuclear charge and mass number, respectively. The ^{14}O events were then separated from those of other oxygen isotopes by making a software selection of events in the correct region of the laboratory momentum-energy (or focal plane position-energy) ($P_L \otimes E_L$) space, since $A \propto P_L^2/E_L$. At a center-of-mass energy of 11.67 MeV, only the ground and first excited states of ^{14}O are kinematically allowed to be populated.

In the second step, we need to determine the trajectories of the ^{14}O particles which have been selected in the ($E_L^2 \otimes R$) and ($P_L \otimes E_L$) spaces in order to separate those $^{14}O_0$ formed directly in $^{1}H(^{14}N, ^{14}O)n$ from those $^{14}O_0$ formed via the γ decay of $^{14}O_1$. Three coordinates are required to describe these trajectories: for instance, P_L and the spherical Θ_L and ϕ_L (where ϕ_L is the azimuthal angle about the beam axis), or P_L and the horizontal and vertical detector entrance angles Θ_x and Θ_y. Since Θ_x is the projection of Θ_L onto the horizontal plane, the angles are related by $\tan(\Theta_L)\sin(\phi_L) = \tan(\Theta_x)$ when ϕ_L is defined as zero for particles emitted in the vertical plane; the vertical angle Θ_y can be similarly defined. Since only two coordinates were measured in this experiment, P_L (or laboratory energy E_L) and Θ_x, an additional hardware mask (described below) was necessary to separate the two ^{14}O groups.

Since the velocity of the center-of-mass frame with respect to the laboratory frame is greater than the velocity of the recoils in the center-of-mass frame for the $^{1}H(^{14}N, ^{14}O)n$ reaction, there is a maximum laboratory recoil angle [15]; this is evident in the angle-energy plot (Θ_L vs E_L), Fig. 3. For those $^{14}O_0$ formed directly, this maximum angle is $\Theta_L = 2.89°$, corresponding to $\Theta_{c.m.} = 94°$; for those $^{14}O_0$ formed after γ decay, this maximum angle is 0.97°, corresponding to $\Theta_{c.m.} = 113°$. For each angle $\Theta_L < 2.89°$, a ground-state ^{14}O can be emitted with two distinct energies, as evident from Fig. 3: a "forward" (high energy) and "backward" (low energy) kinematic solution. The "forward" solution corresponds in the center-of-mass system to a forward-emitted ^{14}O and a backward-emitted neutron; the "backward" solution has these directions reversed.

The determination of the ^{14}O trajectories is complicated by the isotropic recoil distribution in ϕ_L: the ^{14}O's can have a continuum of energies for any given Θ_x. For recoils with $\Theta_x = 0°$, for example, the energy range is 138 MeV < E_L < 168 MeV. Hence if all the recoils were detected, the events from the direct population of the ground state would cover *all* of the area inside the large oval in Fig. 3. This would not allow the weak $^{14}O_1(\gamma)^{14}O_0$ group, which correspondingly would fill the smaller oval, to be separated from the intense $^{14}O_0$'s formed directly.

This problem was overcome by using an entrance aper-

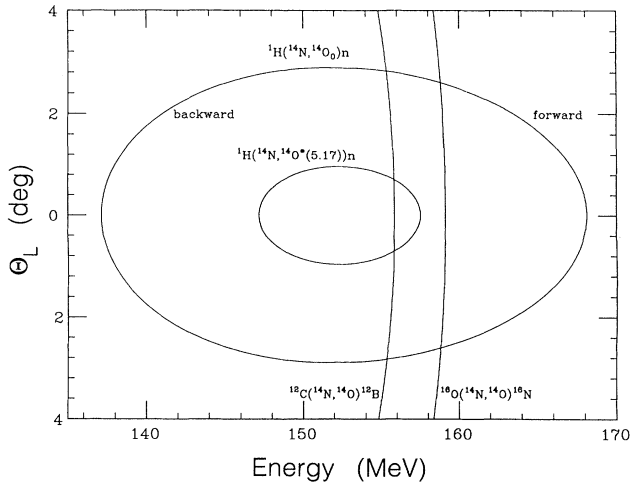

FIG. 3. Variation of energy with laboratory angle Θ_L for the ^{14}O particles from the $^1H(^{14}N, ^{14}O)n$, $^{12}C(^{14}N, ^{14}O)^{12}B$, and $^{16}O(^{14}N, ^{14}O)^{16}N$ reactions. The forward ($\Theta_{c.m.} < 90°$) and backward ($\Theta_{c.m.} < 90°$) solutions are indicated.

ture to the spectrometer which limited the vertical acceptance to $|\Theta_y| \leq 0.74°$ and the horizontal acceptance to $|\Theta_x| \leq 2.43°$. For a given Θ_x, only those events in a limited range of Θ_L will reach the detector with the aperture in place. At $\Theta_x = 0$, for example, only events with $\Theta_L < 0.74°$ reach the detector: this includes nearly all of those $^{14}O_0$ formed after γ decay (which have energies from 146 to 157 MeV), but only those $^{14}O_0$ formed directly which have energies near 138 and 168 MeV. This gave a clean separation of the two ^{14}O groups.

Figure 4 shows a two-dimensional histogram of P_L vs Θ_x for the ^{14}O events that have passed through the $(E_L^2 \otimes R)$ and $(P_L \otimes E_L)$ gates, for one of the 50 data sets measured with a CH_2 target. Since the rectangular aperture prevented those particles which had both a large Θ_y and small Θ_x from reaching the detector (particles which would have fallen into the central region of

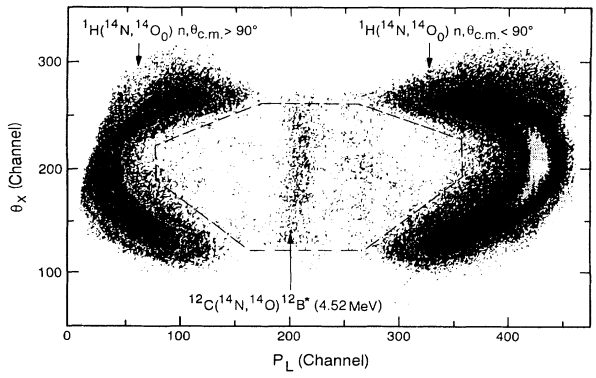

FIG. 4. Logarithmic intensity plot of laboratory momentum vs detector entrance angle ($P_L \otimes \Theta_x$) for the ^{14}O particles, for a typical run. The outer annular shaped group is from the $^1H(^{14}N, ^{14}O_0)n$ reaction, and the dashed line is a software window containing the $^{14}O_1(\gamma)^{14}O_0$ events. A group from the $^{12}C(^{14}N, ^{14}O)^{12}B$ reaction is visible.

the ground-state ellipse in the $P_L \otimes \Theta_x$ distribution), the distribution of the directly formed $^{14}O_0$'s which passed through the aperture has the shape of an annulus in $P_L \otimes \Theta_x$. In contrast, the majority of the $\Theta_L = \pm 1°$ emission cone of the $^{14}O_0$'s formed after γ decay was accepted by the spectrometer, and therefore the excited state ellipse was only slightly affected by the presence of the aperture.

The statistics were too low in any of the individual data sets (of duration 1 hour) to allow the excited-state group to be visible (Fig. 4). The ground-state annulus is visible, along with a group from the $^{12}C(^{14}N, ^{14}O)^{12}B$ reaction; this latter group appears as a vertical line running through the middle of the ellipse (see Fig. 3) because the $^{12}C(^{14}N, ^{14}O)^{12}B$ reaction has a small $dE/d\Theta$. The annulus is not completely connected, because the horizontal opening angle of the spectrometer aperture is 2.43° instead of 3°: particles with the largest angles Θ_x (and thus the largest angles Θ_L when $\phi_L = 90°$) are stopped by the aperture. This divides the ground-state annulus in the $P_L \otimes \Theta_x$ plot into two distinct "lobes," a "forward" (higher P_L) kinematic solution lobe with $0° < \Theta_{c.m.} < 60°$, and a "backward" (lower P_L) lobe with $125° < \Theta_{c.m.} < 180°$. The two lobes are indicated in Fig. 3.

The third step in the analysis involves summing the appropriate peaks in the one-dimensional position (or momentum) spectra of the directly formed $^{14}O_0$ ("ground-state") events and the $^{14}O_1$ $(\gamma)^{14}O_0$ ("excited-state") events to determine the ratio of "ground-state" to "excited-state" events. The momentum spectrum of *all* ^{14}O events gated on the $(E_L^2 \otimes R)$ and $(P_L \otimes E_L)$ windows for all the data sets is shown in Fig. 5(a).

The momentum spectrum of the directly formed $^{14}O_0$'s (the "ground-state" spectrum) is obtained by drawing a more restrictive software gate in Fig. 4 around only the forward lobe of the ground-state annulus. We utilized only events in the forward lobe ($\Theta_{c.m.} < 90°$), because the $^{14}N(p, n)^{14}O_{0,1}$ cross sections [used to convert the ratio from the $^1H(^{14}N, ^{14}O)n$ experiment to an $^{14}O_1$ $\Gamma_\gamma/\Gamma_{tot}$ value] could only be measured for $\Theta_{c.m.} < 90°$. We also utilized events in a software window restricted to $\Theta_x > 0°$, in order to avoid a small leakage of ^{15}O events in the $\Theta_x < 0°$ range; when the full range in Θ_x was used, consistent results were obtained with a higher background. The number of ground-state events in the forward lobe, found by summing the peak in the one-dimensional ground-state momentum, is 3 896 000 ± 2000.

The momentum spectrum of those $^{14}O_0$'s formed after γ decay of $^{14}O_1$ (the "excited-state" spectrum), Fig. 5(b), is obtained from Fig. 4 in an analogous manner to the ground-state spectrum, using a second software window (the dashed line in Fig. 4) lying just inside the ground-state annulus. The determination of the number of excited-state events is made difficult by the presence of a number of peaks from the $^{12}C(^{14}N, ^{14}O)^{12}B$ and $^{16}O(^{14}N, ^{14}O)^{16}N$ reactions in the excited-state spectrum. Peaks were identified by calibrating the focal plane with the known momenta of ^{14}O and ^{15}O groups from the CD_2 target data, and by a comparison with a pre-

vious study of $^{16}O(^{7}Li, ^{7}Be)^{16}N$ at 7 MeV/u (Ref. [16]) which indicated a strong population of the 0.0, 0.297, 3.96, 5.52, and 5.72 levels in ^{16}N, and with a study of $^{12}C(^{12}C, ^{12}N)^{12}B$ at 35 MeV/u which indicated a strong population of the 0.0 and 4.52 levels in ^{12}B [17].

Target thickness and kinematic ($dE/d\Theta$) effects prevented the ^{14}O groups corresponding to $^{14}O_1(\gamma)^{14}O_0$ events from being cleanly separated from ^{14}O groups in the excited-state region of Fig. 4 corresponding to residual states in ^{12}B and ^{16}N. The different energy losses of the incident 175-MeV ^{14}N beam particles and the exiting ^{14}O particles in the 850 $\mu g/cm^2$ CH_2 target [800–1000 keV, or 10–12 channels in Fig. 5(b)] caused most of the spread in ^{14}O energies. The variation of particle energy with angle also spread out the $^{14}O_0$ and $^{14}O_1(\gamma)^{14}O_0$ groups on the focal plane, since $dE/d\Theta$ is very large for these reactions. Although strongly forward peaked, the forward lobe ($\Theta_{c.m.} < 90°$) of those $^{14}O_0$ formed directly extended over 200 channels (17 MeV), and the forward lobe of those $^{14}O_0$ formed after γ decay extended over 60 channels (5 MeV). $dE/d\Theta$ effects added essentially no width to the groups corresponding to ^{16}N and ^{12}B states, since $dE/d\Theta$ is very small for both these reactions at angles near zero degrees. The intrinsic energy widths of the individual states added no significant contribution to the focal plane widths of any of the observed groups.

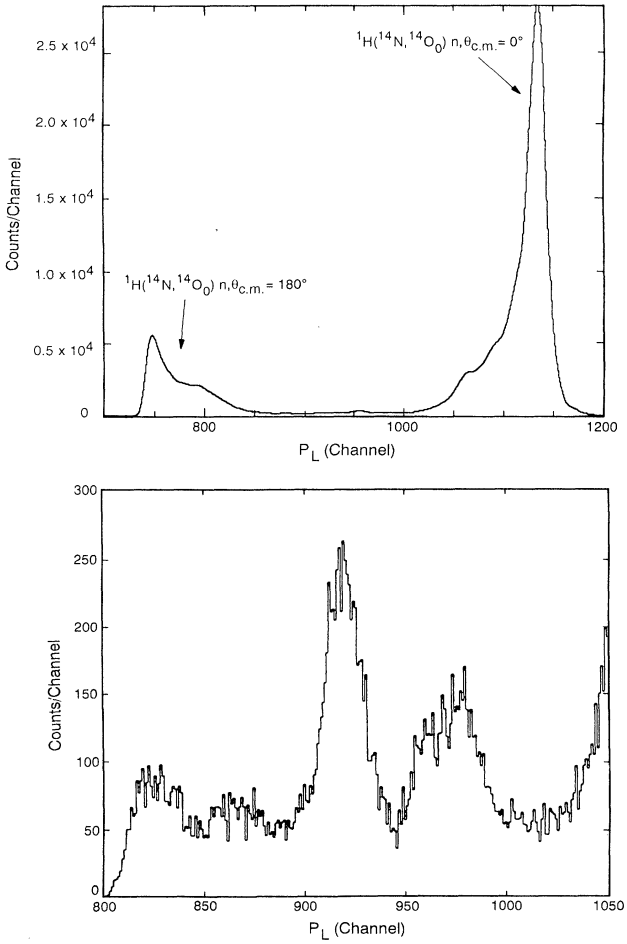

FIG. 5. ^{14}O momentum spectrum P_L for the $^{1}H(^{14}N, ^{14}O)n$ reaction (a) gated on ^{14}O particle identification only, and (b) gated on the software window shown in Fig. 4. The two large peaks at the ends of the spectrum (a) are the $\Theta_{c.m.} = 0°$ and $\Theta_{c.m.} = 180°$ groups from the $^{1}H(^{14}N, ^{14}O_0)n$ reaction.

A comparison of the excited-state momentum spectra from the CH_2 and C target runs is shown in Fig. 6. From the momentum calibration, the $^{14}O_1(\gamma)^{14}O_0$ events are expected to be located on the high-momentum edge of the group corresponding to the $^{12}B_0$ state in the CH_2-target momentum spectrum. We used two methods to extract the number of $^{14}O_1(\gamma)^{14}O_0$ events: (A) subtracting the carbon-target momentum spectrum ("C spectrum") from the CH_2-target momentum spectrum ("CH_2 spectrum") and (B) fitting both momentum spectra with suitable constraints.

Method (A): We began by smoothing the CH_2 and C spectra with a cubic spline routine (which preserved the area to better than 2%) to eliminate small periodic peaks (of spacing $\approx$ 5 channels) appearing throughout the entire position spectra. These peaks result from the discrete PPAC wire structure, and appear when the PPAC is operated at high event rates (>1 kHz).

We next corrected for the different ^{12}B peak widths, caused by the different C and CH_2 target thicknesses, by using a Gaussian smoothing routine on the C spectrum to symmetrically spread the counts in any one position channel into a Gaussian distribution over Λ channels. The width $\Lambda = 10$ channels was chosen to increase the measured 18 channel width of the isolated ^{12}B(4.52 MeV) peak in the C spectrum to the corresponding 20 channel width in the CH_2 spectrum.

We then scaled the C spectrum by the ratio of areas of the ^{12}B(4.52 MeV) group in the CH_2 spectrum and C spectrum, in order to account for total yield (target thickness and integrated beam current) differences. Finally, a constant background was added to the C spectrum to

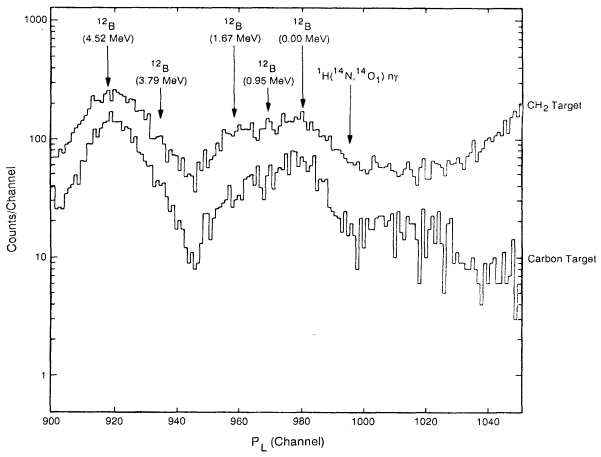

FIG. 6. The ^{14}O momentum spectrum measured with CH_2 and C targets, gated on the ($E_L^2 \otimes R$) and ($P_L \otimes E_L$) software windows.

raise its background level to match the CH_2 spectrum; this shift accounted for the differences in the leakage of the ground-state annulus in the $P_L \otimes \Theta_x$ plot into the gate on this central region for the two spectra. This modified C spectrum was then subtracted from the CH_2 spectrum, and the result is shown in Fig. 7.

There is a peak in this subtracted spectrum at channels 985–1005 which, from the momentum calibration, corresponds to the expected location of the $^1H(^{14}N, ^{14}O_1)n(\gamma)^{14}O_0$ group. The number of counts in the group is 45 ± 24, where the uncertainty corresponds to both counting statistics and an uncertainty of ± 2 counts/channel in the background shift of the C spectrum, and where the $P_L \otimes \Theta_x$ window is restricted to $\Theta_x > 0°$. A consistent number of excited-state counts obtained when the C spectrum was subtracted from the CH_2 spectrum without cubic spline smoothing or Gaussian smearing.

There are other peaks in the subtracted momentum spectrum besides the excited-state group. Because the two targets have different amounts of oxygen contamination, and because the subtraction procedure accounts only for the different amounts of carbon, groups from the $^{16}O(^{14}N, ^{14}O)^{16}N$ reaction (at channels 956, 963, and 1024) do not vanish upon subtraction. Part of the peak at channel 956 is due to leakage of an intense group of ^{16}O events on the focal plane through the software gate; the high intensity of that ^{16}O group gave rise to events with spurious energy signals, some of which fall within the ^{14}O window on the $P_L \otimes E_L$ plot. There is no such ^{16}O leakage between channels 980 and 1005 [the region of interest for the $^1H(^{14}N, ^{14}O)n\gamma$ reaction], but there is a small leakage at channels 1005–1010, which was verified by gating on ^{16}O events in the $P_L \otimes E_L$ plot, keeping the same gate on the $P_L \otimes \Theta_x$ plot, and examining the resulting gated position spectrum.

Method (B): The second method used to determine the number of $^{14}O_1(\gamma)^{14}O_0$ events in the CH_2 spectrum involved fitting the peaks in the CH_2 and C spectra to ^{14}O groups corresponding to known ^{12}B levels in the $^{12}C(^{14}N, ^{14}O)^{12}B$ reaction. A number of constraints were made on the peak positions, widths, and relative areas in order to extract the excited-state events which are on the high-momentum edge of the $^{12}B_0$ peak. We used a quadratic background with an additional exponential tail from the forward angle $^{14}O_0$ group to fit both the C and CH_2 spectra. The two most critical regions for the fit, shown in Fig. 8, are the high-momentum side of the $^{12}B_0$ peak, and the relatively well-isolated ^{12}B(4.52 MeV) peak which was used to constrain the fit to the $^{12}B_0$ peak. The intermediate region in the momentum spectrum, from channels 945–980, contains fifteen ^{16}N levels with excitation energies ranging from 3.36 to 5.52 MeV, and three ^{12}B levels (at E_x =0.95, 1.67, and 2.62 MeV). No attempt was made to fit this region of the momentum spectrum because the relative strengths of these numerous levels are not well known.

One fit constraint was the location of the peak centroids as determined from the momentum calibration. A second constraint was placed on the peak widths. As discussed above, the difference in width of the relatively well-isolated ^{12}B(4.52 MeV) peak in the C and CH_2 spectra is attributable to the different target thicknesses; this width difference was used with the measured width of the $^{12}B_0$ peak in the C spectrum to determine the $^{12}B_0$ peak width in the CH_2 spectrum. A third constraint on the fit is the requirement that the ratio among the areas under the ^{12}B peaks be the same in both the CH_2 and C spectra. In particular, the ratio of areas of the ^{12}B(4.52-MeV) and $^{12}B_0$ levels in the CH_2 spectrum was required to be consistent with the value obtained from the C spectrum.

We then fit the $^{12}B_0$ group in the CH_2 spectrum with all of these constraints and subtracted the fit from the data; the residual 49 ± 10 counts in this region channels (985–1005) were attributed to $^{14}O_1(\gamma)^{14}O_0$ events. The uncertainty is determined from the maximum and minimum values of the $^{12}B_0$ peak which increase the χ^2 value of the fit by 1.0. When a peak of variable area at the location of the $^{14}O_1(\gamma)^{14}O_0$ events was included in the fit with the ^{12}B peaks, the result was 45 ± 20 counts for the $^{14}O_1(\gamma)^{14}O_0$ peak. A complete list of fitting at-

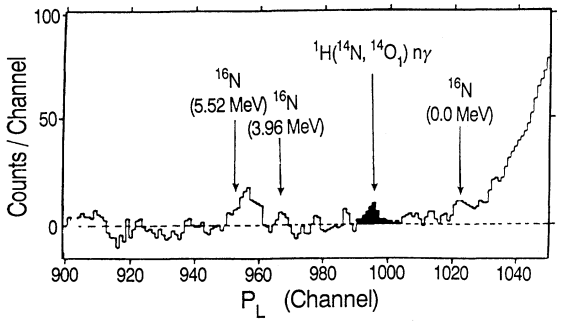

FIG. 7. Momentum spectrum resulting from scaling up and subtracting the smoothed C-target ^{14}O momentum spectrum from the smoothed CH_2-target spectrum.

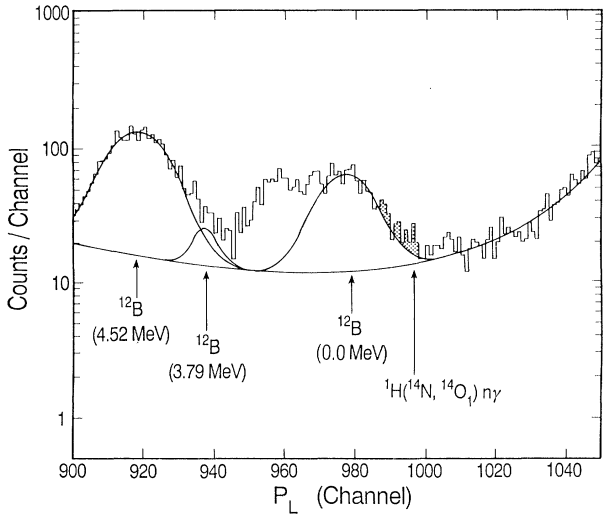

FIG. 8. Gaussian fits to the ^{14}O momentum spectrum, showing only three groups for clarity: $^{12}C(^{14}N, ^{14}O)^{12}B_0$, $^{12}C(^{14}N, ^{14}O)^{12}B^*$(4.52 MeV), and $^1H(^{14}N, ^{14}O_1)n(\gamma)^{14}O_0$.

tempts and their results, for both the positive and full Θ_x angular ranges, and for smoothed and unsmoothed data sets, is given in Ref. [18].

The two methods of (A) subtracting the C and CH_2 spectra and (B) fitting the momentum spectrum give consistent results (45 ± 24 counts) for the number of $^{14}O_0$ particles formed after γ decay. When combined with the number of $^{14}O_0$ formed directly, the ratio of excited-state to ground-state events is (1.16 ± 0.62) $\times 10^{-5}$. This result was then combined with the relative production cross section for $^{14}O_1$ and $^{14}O_0$ (Sec. III) to determine the γ-ray branching ratio of the $^{14}O^*$(5.17-MeV) level in Sec. IV.

III. THE $^{14}N(p, n)^{14}O$ REACTION

A. Experimental setup

For our measurements of the relative cross sections for producing the $^{14}O_0$ and $^{14}O_1$ states via the $^{14}N(p, n)^{14}O$ reaction at $E_{c.m.} = 11.67$ MeV, a 1-μA, 12.5-MeV proton beam was produced at the Seattle FN-Tandem Van de Graaff accelerator, bunched at 4.17 MHz, and chopped to a width of 1.2 ns. The beam passed through a transmission melamine target (3 ± 0.5 mg/cm^2 $C_3H_6N_6$ evaporated onto a 40 μg/cm^2 carbon foil), out the back of the target chamber, and down a 5-m long, lead-lined beam pipe to a heavily shielded beamstop. The beam emittance increased substantially when passing through the target, causing protons to strike the downstream beam pipe and generate a large background neutron flux. This background prevented measurements of $^{14}N(p, n)^{14}O$ neutrons at angles $\Theta_n < 15°$. The angles $\Theta_n > 90°$ were also excluded from our measurement, because the $^{14}N(p, n)^{14}O_1$ cross section was obscured at back angles by the background neutron flux caused by beam particles striking collimating slits located upstream of the target. This second restriction limited our analysis in Sec. IV to the use of the $^1H(^{14}N, ^{14}O)n$ events in the forward kinematic solution ($\Theta_{c.m.} < 90°$).

We detected neutrons with a 12.7-cm-diameter by 5.1-cm-deep cylindrical BC-501 liquid scintillator located 1.4 m from the target, at angles ranging from 15° to 90° from the beam axis. The relative efficiency of the neutron detector as a function of neutron energy E_n was determined by measuring the $^7Li(p, n)^7Be$ reaction at 0° over the proton energy range $2 < E_p < 8$ MeV and comparing the yields with previous absolute cross section measurements [19]. We used targets of 500 μg/cm^2 LiF evaporated onto stopping Ta backings (of thickness 0.005 in) for the efficiency measurement. We used the same detector and electronics for both the $^{14}N(p, n)^{14}O$ and efficiency measurements. A different beamline was used for the efficiency measurement, however, in order to permit the liquid scintillator detector to be placed along the beam axis ($\Theta_n = 0°$) at a distance of 3.85 m from the target. For proton energies E_p <3.5 MeV, the detector was moved closer to the target (to 1.61 m) to prevent wraparound of the T_n spectrum (from the 240 ns beam bunching) while keeping the same settings on the T_n time-to-amplitude converter (TAC) module. We used standard NIM electronics modules to process the neutron time-of-flight (T_n) and neutron energy (E_n) signals for both the $^{14}N(p, n)^{14}O_{0,1}$ angular distribution measurements and the $^7Li(p, n)^7Be$ efficiency measurement [18].

B. Data analysis and results

We separated the neutron and γ-ray signals in the liquid scintillator detector by plotting a signal from a pulse shape discrimination (PSD) module against the scintillator anode signal and drawing separate software windows around the neutron and γ-ray events. Figure 9 shows a typical neutron-gated T_n spectrum from the melamine target at an angle $\Theta_n = 28.5°$ and a flight path of 1.41 m. The tails on the T_n peaks are due to neutron inelastic scattering off of the chamber walls and the asymmetrical time structure of the bunched proton beam. Neutron groups from the $^{14}N(p, n)^{14}O_0$ and $^{14}N(p, n)^{14}O_1$ reactions are seen in this spectrum.

The energy resolution of the time-of-flight system has one contribution from the 1.0–1.2 ns width of the beam pulses, and a second from the active depth of the detector. For the $^{14}N(p, n)^{14}O$ measurement, the contribution of the detector depth to the energy resolution was 7%, while the beam pulse width contribution ranged from 8–30 % for the least and most energetic neutrons, respectively; the total neutron energy resolution for these two cases was 0.040 MeV and 2.00 MeV, respectively, more than adequate to separate the neutrons from the formation of the $^{14}O_0$ and $^{14}O_1$ states.

The neutron detection efficiency was determined with an accuracy of ±10%, the largest contribution from the uncertainty of the $^7Li(p, n)^7Be$ absolute cross sections [19]. The resulting $^{14}N(p, n)^{14}O_{0,1}$ differential cross sections are plotted as a function of neutron angle Θ_n in Fig. 10. The 10% cross section uncertainty is very small

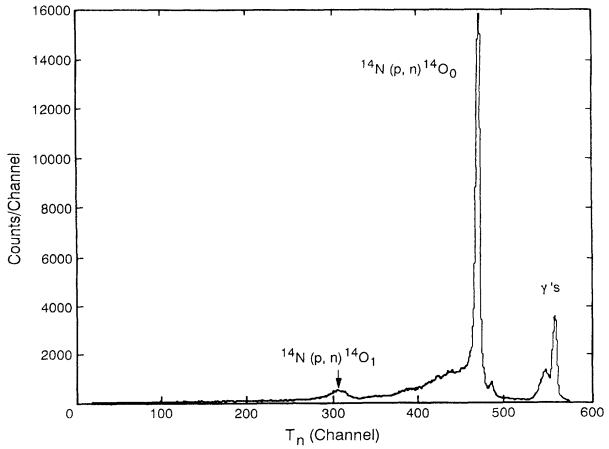

FIG. 9. Gated neutron time-of-flight T_n spectrum for the $^{14}N(p, n)^{14}O$ reaction at $E_p = 12.5$ MeV and neutron angle $\Theta_n = 20.6°$.

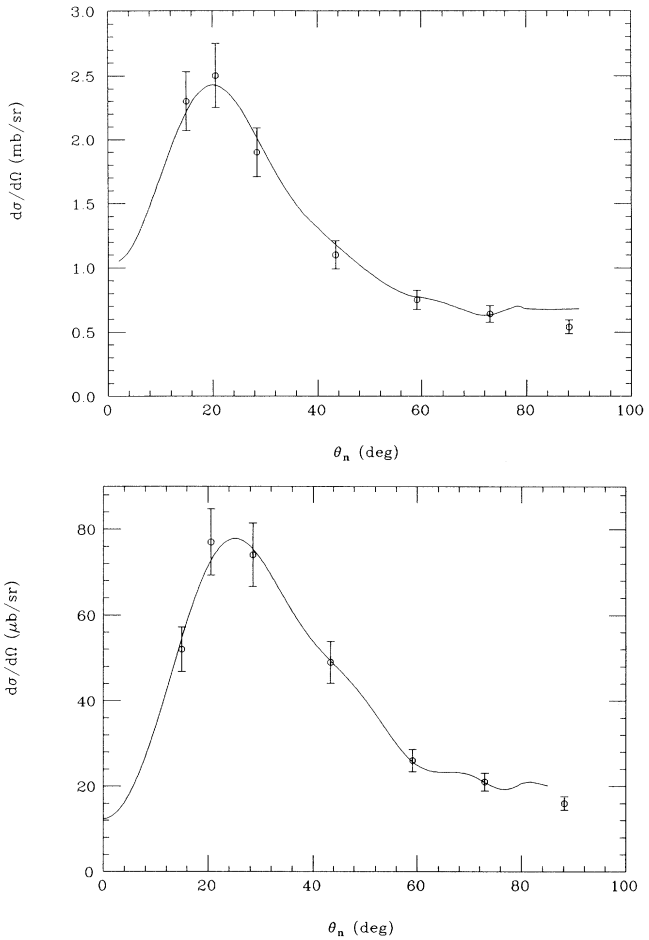

FIG. 10. $^{14}N(p, n)^{14}O_{0,1}$ angular distributions measured from $\Theta_n = 15°$–$90°$, and Legendre polynomial fits.

compared to the 40–50 % uncertainty in the number of $^{14}O_1(\gamma)^{14}O_0$ events measured in the $^1H(^{14}N, ^{14}O)n$ experiment (Sec. II B), and thus does not significantly contribute to the uncertainty in our determination of the branching ratio of the $^{14}O^*$(5.17-MeV) level.

IV. THE $^{14}O^*$(5.17-MeV) γ-BRANCHING RATIO

In order to extract a $\Gamma_\gamma/\Gamma_{tot}$ branching ratio for the $^{14}O^*$(5.17-MeV) state from the results of the $^1H(^{14}N, ^{14}O)n$ measurement described in Sec. II, we need to determine the production cross section ratio restricted to the spectrometer solid angle of the $^1H(^{14}N, ^{14}O)n$ experiment. First, we used Legendre polynomials to fit the $^{14}N(p, n)^{14}O$ angular distributions, as done by Taddeucci *et al.* [20] for this reaction at $E_p = 35$ MeV. Then, we transformed the measured $^{14}N(p, n)^{14}O_{0,1}$ production cross sections, $(d\sigma/d\Omega)_{0,1}(\Theta_n, \phi_n)$, to the inverse-kinematics laboratory frame, $(d\sigma/d\Omega)(P_L, \Theta_x)$. We next determined the momentum distributions of the $^{14}O_0$'s formed directly and of those formed via the γ decay of $^{14}O_1$ in the $^1H(^{14}N, ^{14}O)n$ experiment by integrating these transformed cross sections over Θ_x, weighted with $\sin(\Theta_x)$, and using appropriate limits corresponding to both the spectrometer aperture and the software window used on the $P_L \otimes \Theta_x$ plot as discussed in Sec. II. Finally, we determined the production cross section ratio (ground state to excited state) for the $^1H(^{14}N, ^{14}O)n$ measurement by integrating these momentum distributions over P_L with the appropriate aperture and software cuts.

The first step involved an approximation of the differential cross sections $(d\sigma/d\Omega)_{0,1}$ over the range 0°–15° by using a smooth continuation of the Legendre polynomial fit over the 15°–90° range; the $\sin(\Theta)$ weighting assured that the contribution of these very forward angles to the integral is small, and the uncertainty contributed by this extrapolation is much smaller than the 10% uncertainty in the $(d\sigma/d\Omega)_{0,1}$ over the range $15° < \Theta_n < 90°$. The final two steps utilized a software cut corresponding to the aperture, which omits 75% of the ground-state group and 21% of the excited-state group, and a software cut corresponding to the $P_L \otimes \Theta_x$ software window, which omits 60% of the remaining excited-state events. The small contribution to the uncertainty of the production ratio from the placement of the software and aperture windows is negligible compared to the 10% uncertainty in

TABLE I. Indirect and direct measurements and theoretical predictions of $\Gamma_\gamma/\Gamma_{tot}$.

Ref.	Reaction	$\Gamma_\gamma/\Gamma_{tot}$	Γ_γ (eV)
	Indirect measurements		
[6]	$^{14}N(^3He, ^{14}O)t\gamma$	$\leq 4.0 \times 10^{-4}$	≤ 17.0
[9]	$^{12}C(^3He, n\gamma)^{14}O$	$(7.2 \pm 3.5) \times 10^{-5}$	2.7 ± 1.3
[26]	$^{12}C(^3He, n\gamma)^{14}O$	$\leq 3. \times 10^{-4}$	≤ 11.4
Present	$^1H(^{14}N, ^{14}O)n\gamma$	$(3.1 \pm 1.7) \times 10^{-4}$	12.0 ± 7.0
	Direct measurement		
[10]	$^{13}N(p, \gamma)^{14}O$		3.8 ± 1.2
	Coulomb dissociation measurements		
[11]	$^{14}O(^{208}Pb, ^{13}N\ p)^{208}Pb$		3.1 ± 0.6
[12]	$^{14}O(^{208}Pb, ^{13}N\ p)^{208}Pb$		2.4 ± 0.9
	Theoretical predictions		
[21]			4.1
[22]			2.4
[23]			1.8
[24]			1.5
[25]			1.2

our measured $^{14}N(p, n)^{14}O_{0,1}$ cross sections and the 40–50% uncertainty in the number of $^{14}O_1(\gamma)^{14}O_0$ events. The result is a ground-state to excited-state production cross section ratio of 27 ± 4.

The gamma branching ratio of the $^{14}O^*$(5.17-MeV) level is given by the product of our measured ratio of the number of $^{14}O^*$(5.17-MeV) events to the directly formed $^{14}O_0$ events, (1.16 ± 0.62)× 10^{-5}, and the production cross section ratio, (27 ± 4), giving

$$\Gamma_\gamma/\Gamma_{\rm tot} = (3.1 \pm 1.7) \times 10^{-4}. \quad (4)$$

When combined with the total width of the 5.17-MeV level of 38.1 ± 1.8 keV (Ref. [7]), the γ width is Γ_γ = 12 ± 7 eV and the resonance strength is $\omega\gamma$ = 9 ± 5 eV. This result is listed in Table I along with the previous indirect and direct measurements and a number of model calculations of Γ_γ [21–25]. The present result is substantially larger than, but consistent at the 2-σ level with, the indirect measurement of Fernandez *et al.* [9] (Γ_γ = 2.7 ± 1.3 eV), and is consistent with the upper limits of Aguer *et al.* [26] (Γ_γ < 12 eV) and Wang [6] (Γ_γ < 17 eV).

The weighted mean of the present measurement and the Fernandez *et al.* result is 3.0 ± 1.3 eV. The recent direct $^{13}N(p,\gamma)^{14}O$ measurement of Decrock *et al.* [10] (3.8 ± 1.2 eV) and the ^{14}O-Coulomb dissociation measurements of Motobayashi *et al.* [11] (3.1 ± 0.6 eV) and Kiener *et al.* [12] (2.4 ± 0.8 eV) average to 3.0 ± 0.5 eV; when combined with the indirect measurements, the total weighted mean is Γ_γ = 3.0 ± 0.4 eV. We used this value in the following section to calculate the $^{13}N(p,\gamma)^{14}O$ reaction rate as a function of temperature.

V. THE STELLAR $^{13}N(p, \gamma)^{14}O$ REACTION RATE

Details of the calculation of the stellar $^{13}N(p,\gamma)^{14}O$ reaction rate as a function of temperature are presented in Sec. V of Fernandez *et al.* [9]. The present calculation of the reaction rate, using Γ_γ = 3.0 ± 0.4 eV, is plotted in Fig. 11, and tabulated in Table II, for 0.08≤ T_9 ≤1.0. The $^{14}N(p, \gamma)^{15}O$ and $^{12}C(p, \gamma)^{13}N$ reactions are also plotted in Fig. 11, using rates taken from the compilation of Caughlan and Fowler [27]. It is evident that the $^{13}N(p,\gamma)^{14}O$ reaction is the slowest of all the proton-capture reactions in the CNO and hot CNO cycles for temperatures 0.14 < T_9 < 0.64.

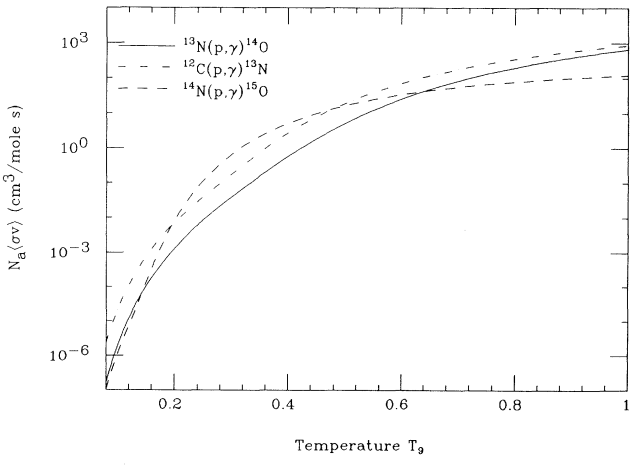

FIG. 11. Total stellar reaction rate $N_A\langle\sigma v\rangle$ as a function of temperature for the $^{13}N(p,\gamma)^{14}O$ reaction from the present work, and the $^{14}N(p, \gamma)^{15}O$, and $^{12}C(p, \gamma)^{13}N$ reactions taken from the compilation of Caughlan and Fowler [27].

The lifetimes of the CNO nuclides against destruction by hydrogen burning are given by (see [2] and [5])

$$\tau = (A_H/X_H)/\rho N_A\langle\sigma v\rangle , \quad (5)$$

where A_H is the atomic mass of hydrogen, X_H is the relative abundance of hydrogen by mass, ρ is the stellar density, and $N_A\langle\sigma v\rangle$ is the appropriate proton-capture reaction rate. The lifetimes for ^{13}N, ^{14}N, and ^{12}C are compared with the ^{13}N, ^{14}O, and ^{15}O e^+-decay lifetimes of 863, 102, and 176 s, respectively, in Fig. 12 for con-

TABLE II. Total stellar reaction rate $N_A\langle\sigma v\rangle$ as a function of temperature for the $^{13}N(p, \gamma)^{14}O$, $^{14}N(p, \gamma)^{15}O$, and $^{12}C(p, \gamma)^{13}N$ reactions.

T_9	$^{13}N(p, \gamma)^{14}O$[a]	$^{12}C(p, \gamma)^{13}N$[b]	$^{14}N(p, \gamma)^{15}O$[b]
0.08	1.63×10^{-7}	2.34×10^{-6}	1.19×10^{-7}
0.09	6.01×10^{-7}	7.54×10^{-6}	4.26×10^{-7}
0.10	1.85×10^{-6}	2.07×10^{-5}	1.28×10^{-6}
0.11	4.95×10^{-6}	5.01×10^{-5}	3.39×10^{-6}
0.12	1.19×10^{-5}	1.10×10^{-4}	8.40×10^{-6}
0.13	2.59×10^{-5}	2.21×10^{-4}	2.06×10^{-5}
0.14	5.26×10^{-5}	4.16×10^{-4}	5.21×10^{-5}
0.15	1.00×10^{-4}	7.40×10^{-4}	1.35×10^{-4}
0.16	1.81×10^{-4}	1.25×10^{-3}	3.43×10^{-4}
0.17	3.13×10^{-4}	2.04×10^{-3}	8.35×10^{-4}
0.18	5.19×10^{-4}	3.20×10^{-3}	1.90×10^{-3}
0.19	8.33×10^{-4}	4.86×10^{-3}	4.04×10^{-3}
0.20	1.30×10^{-3}	7.18×10^{-3}	8.04×10^{-3}
0.21	1.97×10^{-3}	1.04×10^{-2}	1.50×10^{-2}
0.22	2.92×10^{-3}	1.47×10^{-2}	2.65×10^{-2}
0.23	4.23×10^{-3}	2.05×10^{-2}	4.46×10^{-2}
0.24	6.04×10^{-3}	2.83×10^{-2}	7.17×10^{-2}
0.25	8.48×10^{-3}	3.87×10^{-2}	0.111
0.30	3.94×10^{-2}	0.175	0.620
0.35	0.159	0.746	2.06
0.40	0.589	2.70	4.93
0.45	1.91	7.89	9.54
0.50	5.29	19.0	15.9
0.55	12.6	39.1	23.9
0.60	26.4	71.0	33.2
0.65	49.5	117	43.5
0.70	84.9	179	54.4
0.75	135	258	65.6
0.80	203	352	77.0
0.85	289	462	88.3
0.90	395	586	99.3
0.95	521	722	110
1.00	666	868	121
1.05	829	1020	131

[a]Present calculation.
[b]Caughlan and Fowler [27].

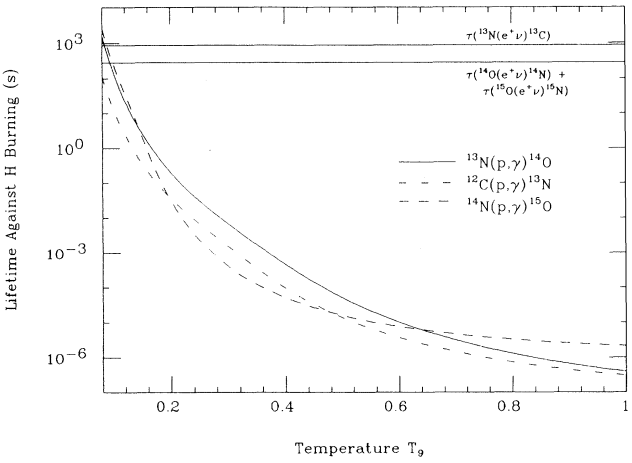

FIG. 12. Lifetime against hydrogen burning via the $^{13}N(p,\gamma)^{14}O$, $^{14}N(p,\ \gamma)^{15}O$, and $^{12}C(p,\ \gamma)^{13}N$ reactions as a function of temperature, and the ^{13}N, ^{14}O, and ^{15}O e^+-decay rates, for a stellar density of $\rho = 5000$ g/cm^3 and a hydrogen mass fraction of $X_H = 0.77$ typical of nova explosions.

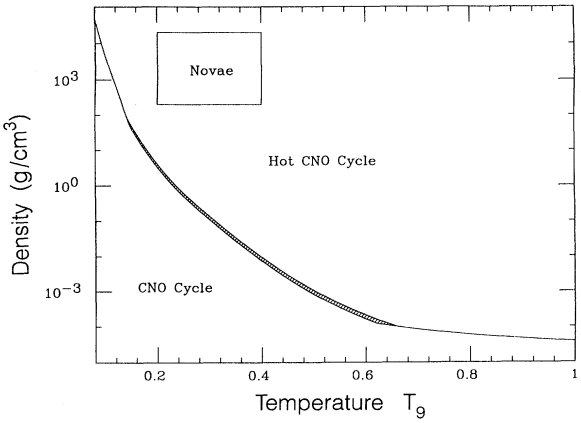

FIG. 13. Density and temperature range for the operation of the hot CNO cycle. The width of the hatched region is due to the remaining uncertainty in Γ_γ for $^{14}O^*$(5.17 MeV). The region typical of nova explosions is also indicated.

ditions typical of nova explosions [28] ($\rho = 5000$ g/cm^3 and $X_H = 0.77$). Significant mass flow through ^{14}O begins to occur at $T_9 = 0.09$, the temperature at which the $^{13}N(p,\gamma)^{14}O$ reaction and $^{13}N(e^+\nu_e)$ decay have equal rates. The onset of the hot CNO cycle occurs at $T_9 = 0.10$, when the rate of the $^{14}N(p,\ \gamma)^{15}O$ reaction, the slowest proton-capture reaction in the hot CNO reaction sequence, exceeds the ^{14}O and ^{15}O e^+-decay rates. At higher temperatures, the energy generation rate of the cycle is limited by the ^{14}O and ^{15}O e^+-decay rates. At $T_9 = 0.10$, the $^{13}N(p,\gamma)^{14}O$ reaction is already 6 times faster than the ^{13}N e^+-decay rate, resulting in 85% of the mass flow going through ^{14}O at the very onset of the hot CNO cycle; this is increased to more than 99% when the temperature reaches $T_9 = 0.14$.

From these results it is evident that the hot CNO cycle will be operating at even the lowest nova temperatures of $T_9 = 0.10$. This results in ^{14}O and ^{15}O being the most abundant nova CNO nuclides, and their e^+-decay products, ^{14}N and ^{15}N, should be enhanced in material ejected from nova explosions [28] and should have a relative isotopic abundance ratio of ~ 1. Observations by Williams and Gallagher [29] of elemental nitrogen enhancements (as well as carbon and oxygen enhancements) in novae ejecta of a factor of $\sim$ 10–100 over solar abundances is consistent with a mixing of carbon-oxygen white dwarf material into the hydrogen accretion layer, resulting in explosive burning via the hot CNO cycle and the production of ^{14}N and ^{15}N.

For the general case, to determine the density-temperature relationship corresponding to the onset of the hot CNO cycle, one equates the sum of the ^{14}O and ^{15}O e^+-decay rates and the lesser of the two proton-capture rates

$$\rho(T) = A_H/[\ (\tau_{14} + \tau_{15})\ X_H\ (N_A\ \langle\sigma v\rangle)_{\rm min}\ ]\ , \qquad (6)$$

where $(N_A\ \langle\sigma v\rangle)_{\rm min}$ includes the temperature dependence of the slowest proton-capture rate in the cycle. The resulting $\rho(T)$ curve is plotted with uncertainties in Fig. 13. If the density and temperature of the stellar environment fall above this curve on the ρ-T plot, then the hot CNO cycle operates. The width of hatched region is due to the remaining uncertainty in Γ_γ for $^{14}O^*$(5.17 MeV). Similar to the calculations of Mathews and Dietrich [22], the present calculation indicates that the hot CNO cycle is turned on at an early stage of a nova explosion. This result may affect the late stages of evolution of supermassive stars (low-density and high temperatures), where an earlier ignition of the hot CNO cycle could generate sufficient energy to prevent the collapse into a black hole [30]. It may also affect the structure and evolution of hypothetical stars with dense neutron cores, where hot CNO cycle and rp-process reactions can occur as quiescent, not explosive, burning in a very hot, dense environment [31].

VI. SUMMARY

We have measured the $^1H(^{14}N,\ ^{14}O)n$ and $^{14}N(p,\ n)^{14}O$ reactions to determine a value of 12 ± 7 eV for the gamma width of the 5.17-MeV level in ^{14}O, consistent with the upper limits of Aguer *et al.* [26] ($\Gamma_\gamma < 12$ eV) and Wang [6] ($\Gamma_\gamma < 17$ eV), and consistent at the 2-σ level with the indirect measurement of Fernandez *et al.* [9] (2.7 ± 1.3 eV). The recent direct $^{13}N(p,\gamma)^{14}O$ measurement of Decrock *et al.* [10] ($\Gamma_\gamma = 3.8 \pm 1.2$ eV) and the ^{14}O-Coulomb dissociation measurements of Motobayashi *et al.* [11] (3.1 ± 0.6 eV) and Kiener *et al.* [12] (2.4 ± 0.8 eV) average to 3.0 ± 0.5 eV; when combined with the indirect measurement average, the total weighted mean is 3.0 ± 0.4 eV. Using this value for the γ width to calculate the $^{13}N(p,\gamma)^{14}O$ stellar reaction rate, it was found in Sec. V that the $^{13}N(p,\gamma)^{14}O$ reaction is the slowest proton-capture reaction in the CNO cycle for temperatures $0.14 < T_9 < 0.64$; and that at nova densities, the mass flow through ^{14}O begins at $T_9 = 0.09$, and the onset of the hot CNO cycle occurs at $T_9 = 0.10$, when the $^{13}N(p,\gamma)^{14}O$ reaction is already 6 times faster than the ^{13}N e^+-decay rate.

ACKNOWLEDGMENTS

The authors would like to thank the staff at ATLAS at Argonne National Laboratory, and the staff of the Nuclear Physics Laboratory at the University of Washington, Seattle, for their assistance in making these measurements. This work was supported by the National Science Foundation and by the Department of Energy.

[1] F. Hoyle and W. A. Fowler, in *Quasi-Stellar Sources and Gravitational Collapse*, edited by I. Robinson, A. Schild, and E. L. Schucking (University of Chicago Press, Chicago, 1965), p. 17.
[2] C. Rolfs and W. S. Rodney, *Cauldrons in the Cosmos* (University of Chicago Press, Chicago, 1988).
[3] G. R. Caughlan, in *CNO-Isotopes in Astrophysics* (Reidel, Netherlands, 1977), p. 121.
[4] C. A. Barnes, in *Proceedings of the Eriche School Nuclear Physics*, edited by Sir Denys Wilkinson (Oxford Pergamon Press, London, 1980), p. 235.
[5] D. D. Clayton, in *Principles of Stellar Evolution and Nucleosynthesis* (McGraw-Hill, New York, 1968).
[6] T. F. Wang, Ph.D. thesis, Yale University, 1986.
[7] T. E. Chupp, R. T. Kouzes, A. B. McDonald, P. D. Parker, T. F. Wang, and A. J. Howard, Phys. Rev. C **31**, 1023 (1985).
[8] F. Ajzenberg-Selove, Nucl. Phys. **A360**, 1 (1981).
[9] P. B. Fernandez, E. G. Adelberger, and A. Garcia, Phys. Rev. C **40**, 1887 (1989).
[10] P. Decrock *et al.*, Phys. Rev. Lett. **67**, 808 (1991).
[11] T. Motobayashi *et al.*, Phys. Lett. B **264**, 259 (1991).
[12] J. Kiener *et al.*, Nucl. Phys. **A522**, 66 (1993).
[13] L. M. Bollinger, Annu. Rev. Nucl. Part. Sci. **36**, 475 (1986).
[14] K. E. Rehm and F. L. H. Wolfs, Nucl. Instrum. Methods **A273**, 262 (1988).
[15] R. Hagedorn, in *Relativistic Kinematics* (Benjamin, New York, 1963), p. 46.
[16] J. Cook, K. W. Kemper, P. V. Drumm, L. K. Fifield, M. A. C. Hotchkis, T. R. Ophel, and C. L. Woods, Phys. Rev. C **30**, 1538 (1984).
[17] J. S. Winfield, N. Anantaraman, S. M. Austin, L. H. Harwood, J. van der Plicht, H.-L. Wu, and A. F. Zeller, Phys. Rev. C **33**, 1333 (1986).
[18] M. S. Smith, Ph.D. thesis, Yale University, 1990.
[19] S. A. Elbakr, I. J. Van Heerden, W. J. McDonald, and G. C. Neilson, Nucl. Instrum. Methods **105**, 512 (1972).
[20] T. N. Taddeucci, R. R. Doering, A. Galonsky, and S. A. Austin, Phys. Rev. C **29**, 764 (1984).
[21] P. Descouvemont and D. Baye, Nucl. Phys. **A500**, 155 (1989).
[22] G. J. Mathews and F. S. Dietrich, Astrophys. J. **287**, 969 (1984).
[23] C. Funck and K. Langanke, Nucl. Phys. **A464**, 90 (1987).
[24] K. Langanke, O. S. van Roosmalen, and W. A. Fowler, Nucl. Phys. **A435**, 657 (1985); **A446**, 750 (1985).
[25] F. C. Barker, Aust. J. Phys. **38**, 657 (1985).
[26] P. Aguer *et al.*, in *Proceedings of the International Symposium on Heavy Ion Physics and Nuclear Astrophysical Problems*, edited by S. Kubuno, M. Ishihara, and T. Nomura (World Scientific, Singapore, 1989), p. 107; C. Rolfs, private communication.
[27] G. R. Caughlan and W. A. Fowler, At. Data Nucl. Data Tables **40**, 283 (1988).
[28] M. Wiescher, J. Gorres, F. -K. Thielemann, and H. Ritter, Astron. Astrophys. **160**, 56 (1986).
[29] R. E. Williams and J. S. Gallagher, Astrophys. J. **228**, 482 (1979).
[30] G. M. Fuller, S. E. Woosley, and T. A. Weaver, Bull. Am. Astronom. Soc. **14**, 947 (1982).
[31] G. T. Biehle, Astrophys. J. **380**, 167 (1991).